CrossMark

A Spectroscopic Search for AGN Activity in the Reionization Era

Nicolas Laporte[1] , Kimihiko Nakajima[2] , Richard S. Ellis[1,2] , Adi Zitrin[3] ,
Daniel P. Stark[4], Ramesh Mainali[4] , and G. W. Roberts-Borsani[1]
[1] Department of Physics and Astronomy, University College London, Gower Street, London WC1E 6BT, UK
[2] European Southern Observatory (ESO), Karl-Schwarzschild-Straße 2, D-85748 Garching, Germany
[3] Physics Department, Ben-Gurion University of the Negev, P.O. Box 653, Be'er-Sheva, 84105, Israel
[4] Steward Observatory, University of Arizona, 933 N Cherry Avenue, Tucson, AZ 85721, USA

Abstract

The ubiquity of Lyman alpha (Lyα) emission in a sample of four bright [O III]-strong star-forming galaxies with redshifts above seven has led to the suggestion that such luminous sources represent a distinct population compared with their fainter, more numerous counterparts. The presence of Lyα emission within the reionization era could indicate that these sources created early ionized bubbles due to their unusually strong radiation, possibly because of the presence of active galactic nuclei. To test this hypothesis, we secured long integration spectra with XSHOOTER on the VLT for three $z \simeq 7$ sources selected to have similar luminosities and prominent excess fluxes in the IRAC 3.6 or 4.5 μm band, usually attributed to strong [O III] emission. We secured additional spectroscopy for one of these galaxies at $z = 7.15$ using MOSFIRE at the Keck telescope. For the most well-studied source in our sample with the strongest IRAC excess, we detect significant nebular emission from He II and N V indicative of a non-thermal source. For the other two sources at $z = 6.81$ and $z = 6.85$, for which no previous optical/near-infrared spectroscopy was available, Lyα is seen in one and C III] emission in the other. Although based on a modest sample, our results further support the hypothesis that the phenomenon of intense [O III] emission is associated preferentially with sources lying in early ionized bubbles. However, even though one of our sources at $z = 7.15$ suggests the presence of non-thermal radiation, such ionized bubbles may not uniquely arise in this manner. We discuss the unique advantages of extending such challenging diagnostic studies with *JWST*.

Key words: early universe – galaxies: distances and redshifts – galaxies: evolution – galaxies: formation – infrared: galaxies – stars: formation
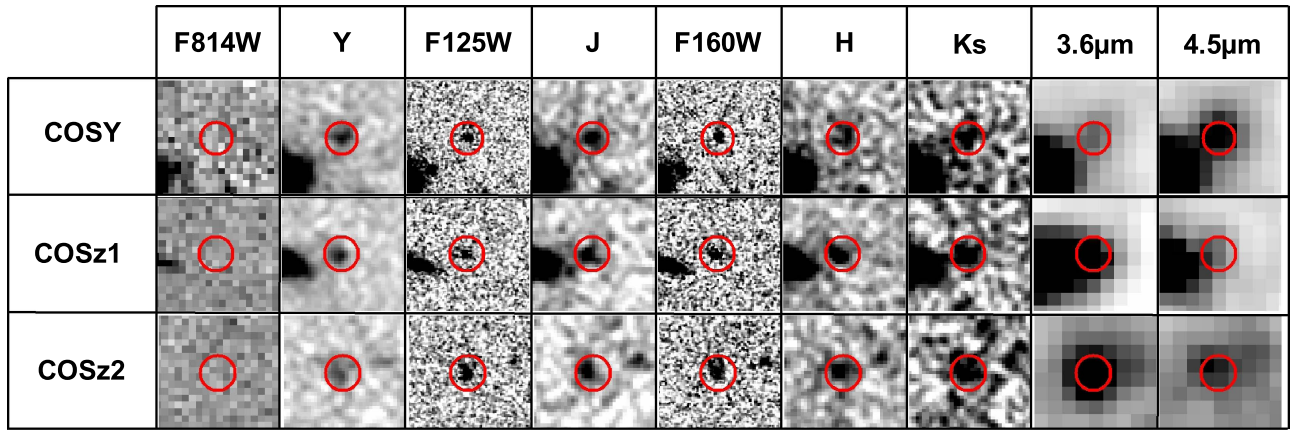
1. Introduction

A fundamental challenge in supporting the now-popular claim that early star-forming galaxies are responsible for cosmic reionization (Robertson et al. 2015; Stark 2016) is the nature and strength of the ionizing radiation emerging from a typical source. To account for the optical depth of electron scattering seen by Planck (Planck Collaboration et al. 2015), at least 10%–20% of the radiation produced by hot main sequence stars below the Lyman limit must escape scattering and absorption by clouds of neutral gas in the circumgalactic medium. Direct measures of this "escape fraction" are not yet possible beyond a redshift $z \simeq 3$, and below which, following considerable observational effort, such a high fraction seems to be quite rare (Nestor et al. 2013; Mostardi et al. 2015; de Barros et al. 2016; Vanzella et al. 2016; Japelj et al. 2017; Rutkowski et al. 2017). Indirect methods based on tracing the extent of low-ionization gas suggest the escape fraction may increase at higher redshift (e.g., Jones et al. 2013; Leethochawalit et al. 2016), but the validity of such methods remains unclear (Reddy et al. 2016; Vasei et al. 2016).

The lack of evidence supporting the efficacy of star-forming galaxies as producers of Lyman continuum radiation into the intergalactic medium (IGM) has led some to suggest that a significant contribution of ionizing radiation may emerge from non-thermal sources such as active galactic nuclei (AGNs) in the nuclei of more massive early galaxies. Assuming 100% of such non-thermal radiation can emerge into the IGM, Madau & Haardt (2015) demonstrate that, depending on the uncertain faint end portion of the high-redshift AGN luminosity function (Glikman et al. 2011; Giallongo et al. 2015; Mitra et al. 2018;

D'Aloisio et al. 2017), a significant fraction of the late-ionizing contribution may arise in this manner. While it seems unlikely that early AGNs can dominate the reionization process, such a contribution could alleviate the requirement from star-forming galaxies. Of course, given that quasars with supermassive black holes are seen to redshifts of at least $z \simeq 7$, it seems reasonable to assume there are earlier galaxies containing nuclear black holes.

Possible evidence in support of a contribution of ionizing radiation from non-thermal sources follows the surprising discovery of Lyman alpha (Lyα) emission in all four $7.15 < z < 8.68$ sources selected by Roberts-Borsani et al. (2016) (hereafter RBS) on the basis of their high UV luminosity *and* the presence of intense [O III] 5007 Å emission as inferred from a prominent excess signal in the IRAC 4.5 μm band. This visibility of Lyα emission in [O III]-enhanced objects contrasts with the significant decline in the presence of the line in the general population of $z \sim 6$–7 LBGs (e.g., Schenker et al. 2012; Pentericci et al. 2014).

Spectroscopic followup of this unique sample (Oesch et al. 2015; Zitrin et al. 2015; Stark et al. 2017) not only revealed ubiquitous Lyα emission at a time when the IGM is thought to be 60% neutral, but it also revealed other UV nebular emission lines such as C III 1909 Å. Stark et al. (2017) suggest these [O III]-strong luminous examples may have created early ionized bubbles in the IGM thereby enabling Lyα photons to escape. Although Stark et al. proposed several different hypotheses for the visibility of Lyα in these sources, the most intriguing explanation posits that these luminous sources harbor AGN.

Figure 1. Thumbnail images of the three $z \sim 7$ targets observed with XSHOOTER/VLT. Each stamp is $5.''5 \times 5.''5$, the position of each candidate is displayed by a red $0.''8$ radius circle.

The present paper is concerned with a detailed a spectroscopic investigation of this hypothesis. Emission lines such as C III] 1909 Å, He II 1640, C IV 1550, and N V 1240 Å can be used as valuable diagnostics of the underlying radiation field (e.g., Feltre et al. 2016; Gutkin et al. 2016; Mainali et al. 2017). Although it is challenging to detect these weaker lines with the necessary precision, we have selected three bright sources with IRAC excesses at $z \simeq 7$ for a diagnostic study.

A plan of the paper follows. In Section 2 we discuss the selection of our three targets, one of which is drawn from the earlier RBS sample. We also discuss the various spectroscopic campaigns. The bulk of our data comes from deep exposures with VLT's XSHOOTER which has the unique advantage of simultaneous coverage of the bulk of the interesting emission lines. We also discuss the reduction of the data. In Section 3 we discuss the basic properties of our sources based on SED-fitting and the known spectroscopic redshifts. In Section 4, we discuss the emission-line spectra for each of the sources in turn, and in Section 5 use photoionization codes to test for the present of non-thermal radiation in our sample. We summarize our results in Section 6 in the context of future work.

Throughout this paper, a concordance cosmology is adopted, with $\Omega_\Lambda = 0.7$, $\Omega_m = 0.3$ and $H_0 = 70 \text{ km s}^{-1} \text{ Mpc}^{-1}$. All magnitudes are given in the AB system (Oke & Gunn 1983).

2. Target Selection and Observations

The goal of the paper is to determine whether the more luminous sources in the reionization era with prominent [O III] excesses as detected with IRAC, reveal evidence of AGN activity as determined from rest-frame UV spectroscopy.

The selection of an IRAC excess source is normally done in addition to the now-standard Lyman break technique. The detectability of an implied [O III] excess signal in either the IRAC 3.6 or 4.5 μm photometric band restricts the redshift range of targets. As discussed by Smit et al. (2015), [O III] will be present in the 3.6 μm band and display an excess compared to 4.5 μm only when Hα does not lie in the latter band. This means a [O III] excess is optimally revealed for a narrow redshift range $6.6 < z < 6.9$ corresponding to the end of reionization. By contrast, a [O III] excess in the 4.5 μm band does not suffer from an additional line in the 3.6 μm (except a likely weaker [O II] 3727 Å for $z > 7.6$). In this respect, a 4.5 μm excess arising from [O III] is visible over $7 < z < 9$ (Roberts-Borsani et al. 2016).

However, there is a second consideration in the spectroscopic followup of such candidates, namely the visibility of the key diagnostic high ionization potential metal lines (Stark et al. 2014). The most valuable indications of AGN activity are the lines of C IV 1550, He II 1640, and N V 1240 Å (Feltre et al. 2016). With ground-based spectrographs, not all these lines are well-placed between $z \simeq 7.3$ and 8.

The present sample was chosen on the basis of its visibility from ESO's Very Large Telescope (VLT) as well as maximizing the chance of detecting multiple high ionization lines at $z \simeq 7$. From the four RBS targets discussed in Stark et al. (2017), we therefore selected the bright ($H_{160} = 25.1$) target COS-zs7-1 with a confirmed spectroscopic redshift of $z = 7.154$, which has the largest 4.5 μm excess in the RBS list. In what follows, we refer to this Y-band drop out as COSY.

To this, we added the two brightest sources drawn from the list of 3.6 μm excess objects published by Smit et al. (2015), namely COS-3018555981 ($H_{160} = 24.9$, $z_{\text{photo}} = 6.76$) and COS-2987030247 ($H_{160} = 24.8$, $z_{\text{photo}} = 6.66$). As these are z-band dropouts, for convenience we refer below to these as COSz1 and COSz2 (Figure 2), respectively.

Although neither Smit et al. (2015) target was spectroscopically confirmed at the time this project was conceived, we considered the narrow redshift window for an excess in the 3.6 μm band to be a convincing indication. Subsequently (and fortunately), both sources were spectroscopically confirmed via [C II] 158 μm detections at $z = 6.85$ and 6.81 respectively, with ALMA (Smit et al. 2017).

All three targets lie in the COSMOS field, thus there is excellent photometry from both the CANDELS (Grogin et al. 2011; Koekemoer et al. 2011) and UltraVISTA (McCracken et al. 2012) surveys. To aid our analyses, we collated all the images containing the three candidates using the public CANDELS[5] (version 1) and UltraVISTA surveys[6] (version 3) catalogs. We added two images from the deep Spitzer-CANDELS survey (Ashby et al. 2015) at 3.6 and 4.5 μm. Thumbnail images of our three targets in the various bands are shown in Figure 1 and our derived photometry is in Table 1.

---

5 https://candels.ucolick.org/
6 http://www.ultravista.org/

Table 1
Photometry of the Three Selected Targets

ID	F814W	Y	F125W	J	F160W	H	Ks	3.6 μm	4.5 μm
COSY	>30.1	25.09 ± 0.14	25.25 ± 0.13	25.11 ± 0.17	25.32 ± 0.17	25.47 ± 0.30	25.35 ± 0.37	25.09 ± 0.59	23.92 ± 0.32
COSz1	>29.4	25.43 ± 0.19	25.35 ± 0.15	25.31 ± 0.21	25.09 ± 0.14	25.18 ± 0.23	25.12 ± 0.30	23.90 ± 0.30	25.20 ± 0.60
COSz2	>29.4	25.53 ± 0.21	24.85 ± 0.1	25.43 ± 0.23	25.38 ± 0.18	25.30 ± 0.26	25.06 ± 0.28	24.11 ± 0.45	24.39 ± 0.48
COSz2*	>29.4	26.76 ± 0.37	26.89 ± 0.32	26.40 ± 0.32	25.79 ± 0.13	25.64 ± 0.21	26.01 ± 0.38	...	...

Note. Non-detections are at 2σ in a $0\!''4$ radius aperture at the object's position.

Table 2
Photometric Redshift Estimates Obtained Using
Different SED-fitting Approaches: *Hyperz* uses a χ^2 Minimization Method and
BPZ Uses a Bayesian Procedure

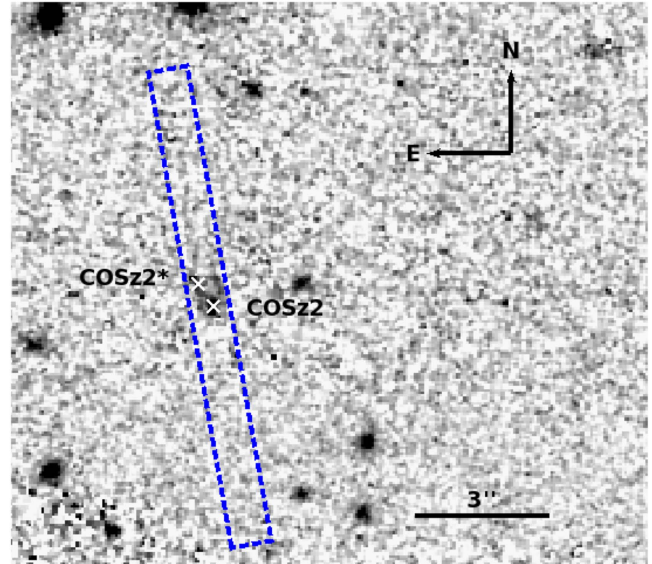| ID	*Hyperz*			*BPZ*			z_{spec}
	z_{phot}	χ^2	1σ	z_{phot}	χ^2	1σ	
COSY	7.06	0.67	6.21–7.21	6.95	1.12	6.17–7.73	7.149
COSz1	6.84	1.26	6.25–7.21	6.90	0.74	6.12–7.68	6.854
COSz2	6.61	1.71	6.08–7.46	6.88	1.43	6.11–7.65	6.816
COSz2*	2.16	1.21	2.01–2.81	1.50	0.76	1.14–8.32	2.11

2.1. VLT Spectroscopy

Our primary spectroscopic program was carried out with XSHOOTER/VLT (Vernet et al. 2011) in service mode (ID: 097.A-0043, PI: R. Ellis) between 2016 April and 2017 March at an average airmass of $\sim$1.2 and in good seeing conditions $\sim$0$''$7. Using blind offsets, observations were undertaken via A and B nodding positions 4 arcsec apart with a 0.9 arcsec slit. Because the three XSHOOTER arms gather data independently, to maximize the key near-infrared exposures times, we adopted a unit 600 s exposure, with 580 s and 560 s in the VIS and UVB arms, respectively. The total on-source exposure time is 11h 20 m (40.8 ks) for COSz1 and COSz2, and 12h (43.2 ks) for COSY.

We reduced the XSHOOTER data using the ESO Reflex software (version 2.8—Freudling et al. 2013) together with the XSHOOTER pipeline (version 2.8.4). We first reduced all exposures on a given target with a master flat combining all flat exposures acquired during the same run. We also reduced all exposures with calibration data acquired during the same night, and combined all reduced exposures with the imcombine task in IRAF. Tests demonstrated both resulting 2D spectra are similar, and in the following we extract and analyze emission lines from spectra obtained with the first procedure.

2.2. Keck Spectroscopy

In a separate campaign (PI: A Zitrin), COSY was also studied in the J band using the MOSFIRE (McLean et al. 2012) multi-slit spectrograph at the Keck observatory on 2016 May 1 and 2. A 0.7 arcsec wide slit was placed on COSY and the observations were carried out in 120 s unit exposures with an AB dithering pattern of ±1.5 arcsec along the slit. Among other objects, another slit in the same mask was placed on a nearby star to monitor possible drifts and changes in seeing and transparency. Exposure times of 1.8 and 2.6 hr on the first and second night, respectively, were obtained, for a total integration time of 4.4 hr. The average airmass during the observations was $\sim$1.2, the average seeing 0.7 arcsec, and the conditions clear.

Figure 2. Detailed *Hubble Space Telescope (HST)* F160W image of the target COSz2 target indicating the presence of the companion COSz2* 0.7 arcsec to the NE whose photometric and spectroscopic properties suggest it is a foreground object (Table 2). The centroid of each object is displayed by the white cross; the position of the XSHOOTER slit is displayed by the dashed blue box.

The MOSFIRE data were reduced using the standard MOSFIRE reduction pipeline,[7] which includes flat-fielding, wavelength calibration, background subtraction, and combining individual exposures for each slit on the mask. The output yields a reduced 2D spectrum per slit per night, along with its error and S/N . The combined 2D spectrum was obtained by inverse-variance weighting the resulting 2D spectra from the two nights.
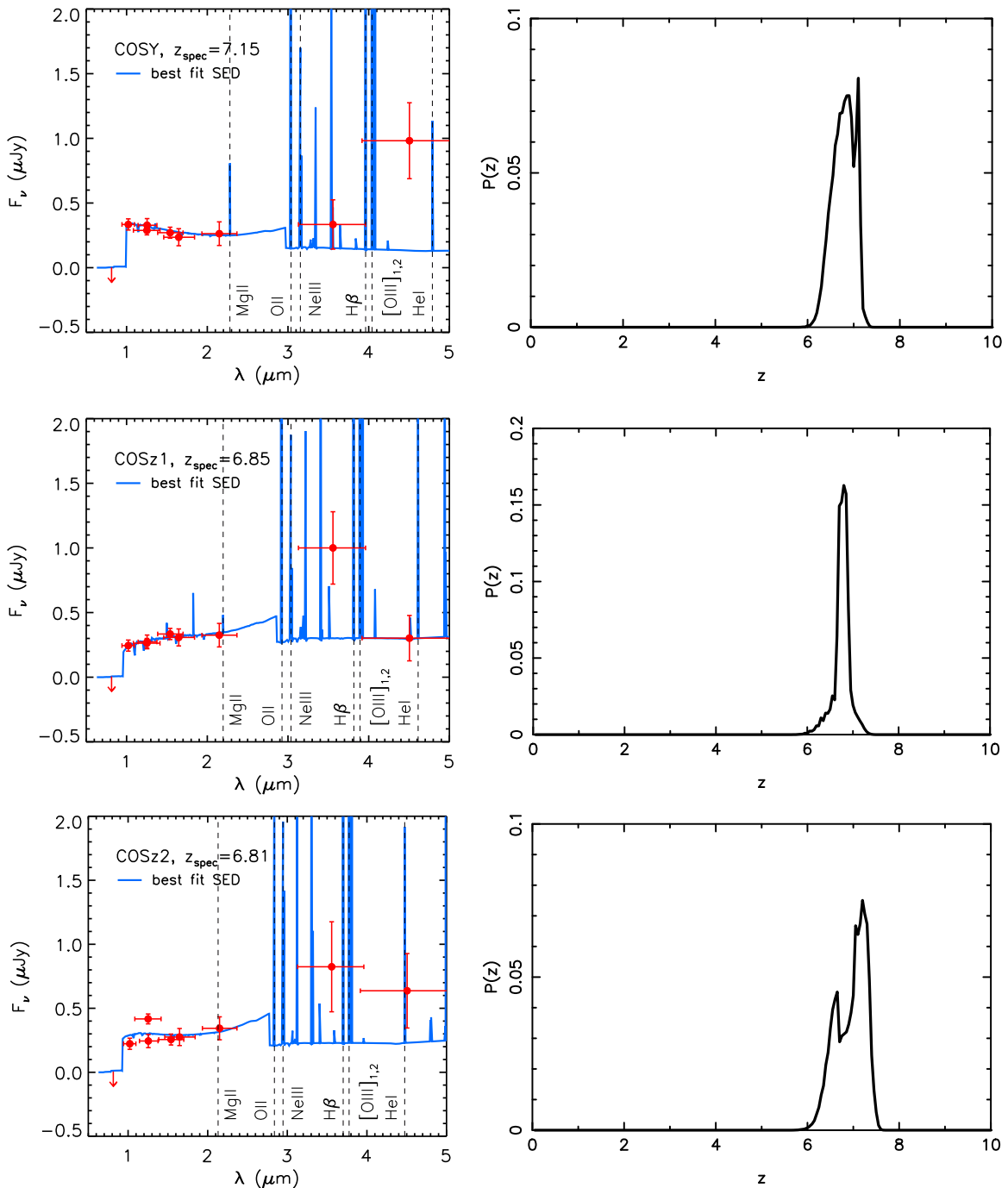
3. Physical Properties

Before we discuss the spectroscopic diagnostics (Section 4), we review the physical properties of our three [O III]-strong sources so as to place them in the context of other sources being targeted in the reionization era.

Adopting the spectroscopic redshifts, we use the SEDs to determine their important physical properties, namely stellar masses, star formation rates (SFRs), and UV luminosities, M_{UV}. This allows us to consider them in the context of other sources being surveyed in the reionization era. We begin by using the *MAGPHYS* (da Cunha et al. 2008) code. Because this code does not take into account the possibility of contamination by nebular emission, we ignore the photometry in the relevant IRAC band. We find that all targets have stellar masses ranging

---

7 http://www2.keck.hawaii.edu/inst/mosfire/drp.html

Figure 3. Left: spectral energy distribution of the three targets. Right: photometric redshift likelihood functions (see the text for details).
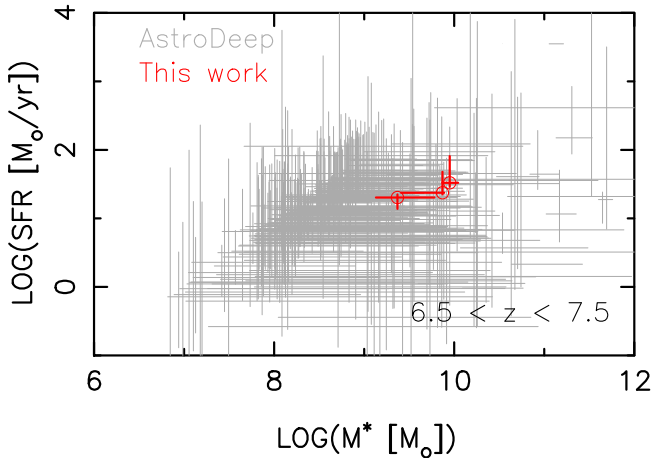
from 0.19 to 1.1×10^{10} $M_\odot$, SFRs ranging from 20 to 33 $M_\odot$ yr^{-1} and dust contents with A_V ranging from 0.3 to 0.9 mag.

To consider more carefully the influence of the inferred [O III] emission line in the IRAC photometry on the derived stellar mass, we next use *Hyperz* with the Starburst99 library (Leitherer et al. 1999) again adopting the spectroscopic redshift (Figure 3). Assuming an age prior of >10 Myr, we now find the stellar masses range from 2.3 to 8.9×10^9 $M_\odot$. To place our targets in context with the general population of objects at $z \sim 7$, we make use of the AstroDeep catalogs publicly available for four of the six Frontier Fields (Di Criscienzo et al. 2017; Merlin et al. 2016; Castellano et al. 2016). We

compare our sources with all sources from this catalog with $6.5 < z_{phot} < 7.5$, which have been well fitted ($0.5 < \chi^2_{reduced} < 2.0$) and with a narrow redshift probability distribution ($\Delta z < 1.0$). In Figure 4, we plot the SFRs and stellar masses of our three targets comparing them with those in the AstroDeep population. As seen, we are probing the properties of the most massive objects at $z \sim 7$. We also estimated physical sizes using the half light radius measured by SExtractor on the F160W *HST* image (following the method of Oesch et al. 2010). These range from 0.3 to 1.0 kpc consistent with results by Oesch et al. (2010), Kawamata et al. (2015), and Laporte et al. (2016). Therefore, they display a specific SFR of $3–9 \times 10^{-9}$ yr^{-1} which is consistent with

Table 3
Physical Properties Deduced from the SEDs and Spectroscopic Redshifts

ID	R.A. [J2000]	Decl. [J2000]	z_{spec}	$M_\star$ $\times 10^9 M_\odot$	SFR $M_\odot\,yr^{-1}$	A_v [mag]	$r_{1/2}$ [kpc]	M_{UV}	UV Slope
COSY	150.09904	2.3436043	7.149	$2.34^{+3.69}_{-0.99}$	$20.2^{+2.2}_{-6.4}$	$0.3^{+0.3}_{-0.1}$	0.33 ± 0.03	-21.8 ± 0.2	-2.33 ± 0.03
COSz1	150.12575	2.26661	6.854	$7.41^{+0.35}_{-4.84}$	$23.7^{+24.2}_{-1.3}$	$0.8^{+0.1}_{-0.4}$	0.79 ± 0.21	-21.6 ± 0.2	-1.18 ± 0.19
COSz2	150.12444	2.21729	6.816	$8.91^{+1.56}_{-2.15}$	$33.1^{+48.2}_{-4.2}$	$0.3^{+0.4}_{-0.1}$	0.96 ± 0.20	-22.1 ± 0.1	-1.72 ± 0.43

Figure 4. The star formation rate and stellar mass of the three targets (in red) are compared with those of well-fitted $z \sim 7$ objects in the AstroDeep catalogs (in gray) for four of the Frontier Fields (Castellano et al. 2016; Merlin et al. 2016; Di Criscienzo et al. 2017). Clearly, the targets represent the most massive and actively star-forming sources at these redshifts.

those previously published by Stark et al. (2013), Duncan et al. (2014) and Lehnert et al. (2015). We also compute the UV slope β following the precepts of Bouwens et al. (2014). There is quite a variation within our sample with COSz1, and to a lesser extent, COSz2, significantly redder than COSY and the general population. Our β values are however within the range found for the general LBG population in this redshift interval. Song et al. (2016) measure $\beta = -2.2^{+0.3}_{-0.2}$ for an object with $M_{uv} = -21.3$, similar to COSY; Stark et al. (2017) find $\beta = -1.5$ in a $M_{uv} = -21.7$ galaxy similar to COSz1; Oesch et al. (2015) determine $\beta = -1.7 \pm 0.1$ in a $M_{uv} = -22.06$ object similar to COSz2.

We summarize these physical properties in Table 3. We take the unusual step of adopting the *Hyperz* derivations for the stellar mass and photometric redshift (as that code takes account of [O III] contamination of the IRAC photometry), while using *MAGPHYS* results for the SFR and reddening (as these parameters are unaffected by line contamination, and it has been demonstrated in da Cunha et al. (2008) that this code more accurately reproduces these parameters via its exploration of several dust extinctions laws).
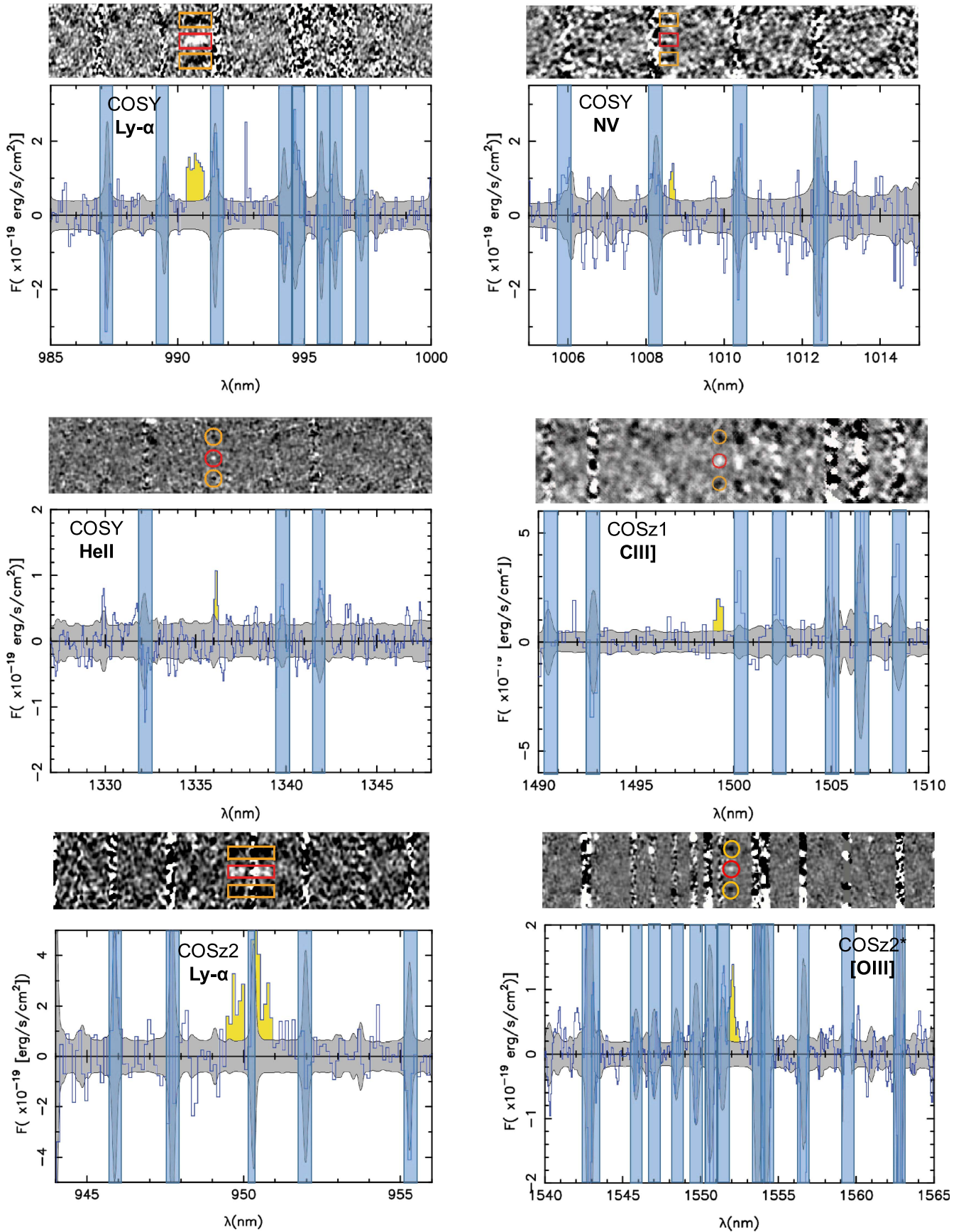
4. Emission-line Detections

All three targets are massive sources with intense star formation rates, so we now examine the nature of their radiation fields as well as to explore whether, as was the case for the four RBS [O III]-excess sources, the newly studied sources also show prominent Lyα emission. We discuss the emission-line content of the spectra of each target in turn based both on a visual inspection of the 2D spectra, and the 1D
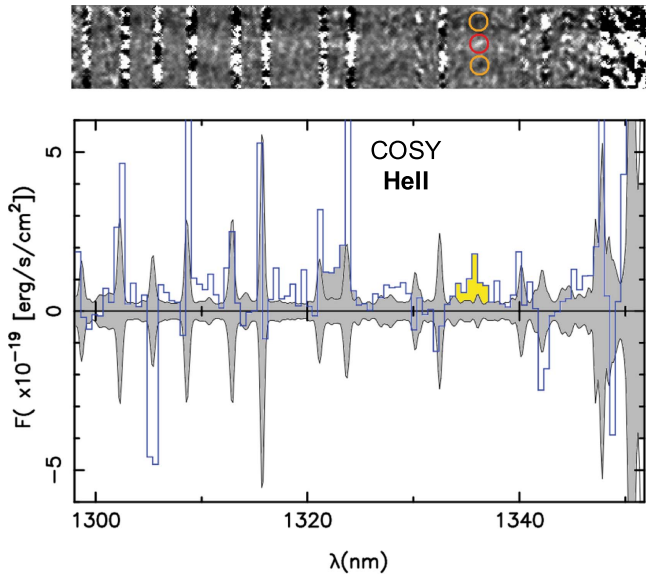
extracted spectrum at the relevant target position within the slit. Recognizing that the reliable detection of faint diagnostic lines is challenging even with these long integration times, we verified the credibility of weak lines by examining the two independent half exposures and, in the specific case of COSY, comparing the XSHOOTER and MOSFIRE spectra where they overlap in wavelength. In the following discussion, errors on line fluxes and upper limits were determined by considering the rms in adjacent regions using a rectangular aperture set by the width of typical nebular lines (12 pixels for XSHOOTER) and the spatial extent set by the seeing (3 pixels). We also compared these values with those estimated from the 1σ error estimated by *Reflex* (see below for details), and found that both estimates are consistent. The relevant line detections are collated and displayed in Figure 5.

4.1. COSY

Stark et al. (2017) already detected prominent Lyα emission at $z = 7.15$ in this target on the basis of a 4-hr exposure with MOSFIRE. Furthermore, deep ALMA observations provide an additional detection of [C II] 158 μm (Pentericci et al. 2016). With the deeper XSHOOTER data, we recover Lyα at 9907.2 Å with significantly improved signal to noise. We note it is reasonably broad with a rest-frame FWHM of 211 ± 55 km s^{-1}, larger than that found, for example, by Zitrin et al. (2015) for a similar [O III]-strong source at $z = 8.68$ (FWHM = 117^{+94}_{-66} km s^{-1}). Additionally, we detect two further emission lines at 10 086.4 Å and 13 360.3 Å, which we identify as N V 1240 Å and He II 1640 Å, respectively. Both new lines are significant at $\approx 5\sigma$ with rest-frame equivalent widths (EWs) of $3.2^{+0.8}_{-0.7}$Å and $2.8^{+1.3}_{-0.9}$Å, respectively, for N V and He II. However, given the position of N V close to the edge of the XSHOOTER visible arm, the noise level is strongly varying with wavelength, so the level of significance depends somewhat on the placement of apertures for estimating the noise level. However, the reliability of the line is confirmed by the detection in two independent exposures sharing the total exposure time. The second counterpart of the N V doublet is not seen in our data above a level of 1.33×10^{-18} cgs, suggesting a flux ratio between the two counterparts of N V]1238/N V]1242 > 1.05, which is consistent with previous findings (Torres-Peimbert & Pena 1984; Kuraszkiewicz & Green 2002). A potential detection at 9927 Å is rejected due to the absence of negative counterparts. We estimate a Lyα EW = $27.5^{+3.8}_{-3.6}$, which is consistent with previous findings by Stark et al. (2017) and a velocity offset of $\Delta \nu_{Ly\alpha} = 286.6$ km s^{-1}, based on a previous [C II] detection from Pentericci et al. (2016). Such an offset is similar to those observed in $z \geqslant 6.5$ spectroscopically confirmed galaxies. The limited overlap in wavelength between the independent MOSFIRE spectrum and that of XSHOOTER allows us to confirm the He II 1640 Å emission at $\lambda = 13357$ Å with a flux of $(1.20 \pm 0.45) \times 10^{-18}$ erg/s/cm^{-2}, consistent with the XSHOOTER data (Figure 6). Although the line is

Figure 5. For each panel, we show the XSHOOTER 2D spectrum (upper), revealing the two negative counterparts with the central positive and (lower) the extracted 1D-spectrum (blue) with the 1σ rms (gray). Top left: Lyα emission line detected in COSY. Top-right: N V emission in COSY. Center left: He II emission in COSY, Center-right: [C III] in COSz1. Bottom left: Lyα in COSz2. Bottom right: [O III] in COSz2*.

Figure 6. As in Figure 5, but for the He II emission line detected in the COSY spectrum obtained with MOSFIRE.

seen independently with both instruments, it is narrow with an observed line width (FWHM$_{\text{X-Shooter}}$ = 1.8 Å and FWHM$_{\text{MOSFIRE}}$ = 3.8 Å) comparable with the resolution of each spectrograph ($R_{\text{X-Shooter}}$ = 5410 and R_{MOSFIRE} = 3270).

4.2. COSz1

Only one emission line at $\lambda = 14\,992$ Å is seen in this source over the full wavelength range covered by XSHOOTER. The line appears to be robust with a ≈4σ significance ($f_{\text{C III}}$ = 1.33 ± 0.31 cgs, rest-frame EW = $4.0^{+2.2}_{-1.5}$ Å). Adopting the ALMA redshift from Smit et al. (2017), the likely identification is C III] 1909 Å at $z = 6.854$. In this case, normally we would expect to see the 1907 Å companion in the doublet at 14 977 Å because the night sky spectrum is relatively clear at this wavelength. The 1907/1909 Å flux ratio is typically ≃1.0–1.5 at intermediate redshifts. Our non-detection of C III] 1907 implies a flux ratio of <0.6 at 3σ. This could imply a very high gas density. Upper limits are tabulated for the other diagnostic lines in Table 4; that for Lyα is particularly stringent.

4.3. COSz2

We detect two reasonably convincing emission lines in the COSz2 XSHOOTER spectrum at $\lambda = 9502.0$ Å (S/N ∼ 3) and $\lambda = 15520$ Å (S/N ∼ 7.0). However, we cannot find any association at the same redshift for these two lines, and therefore, noting the double structure of COSz2 discussed in Section 3, examined whether the lines may belong to two independent sources. Assuming that the bluer line is Lyα, the redshift of COSz2 would be $z = 6.816$ with a rest-frame EW = $16.2^{+5.2}_{-5.5}$ consistent with a velocity offset $\Delta_\nu = 325.6$ km s^{-1} comparable with previous findings given the ALMA redshift. As in the case of COSY, Lyα appears unusually broad compared to other detections at this redshift (rest-frame FWHM = 506 ± 55 km s^{-1}). Unfortunately, some of the other diagnostic lines (such as He II, C III]) would be hard to detect at this redshift, as they would lie close to, or be obscured by, a night sky line. It seems likely that the second line is associated with the nearby companion, COS z2*. If this

line is [O III] 5007 Å the redshift would be be $z = 2.099$ and its weaker 4959 Å component would fall under a sky line. Although the photometric redshift is uncertain ($z_{\text{phot}} = 2.16^{+0.65}_{-0.15}$), the identification is consistent.

5. Photoionization Modeling

In summary, our spectra reveal Lyα emission for two of our 3 IRAC excess targets weakening slightly the ubiquity of emission that was so striking in the earlier RBS sample. However, we see evidence for non-thermal radiation field in one source and possibly a harder radiation field than typical at lower redshift in a second. The spectrum of COSY is particularly intriguing, with convincing detections of N V and He II. COSz1 also shows a convincing C III] emission as was found by Stark et al. (2017) for the $z = 7.73$ source EGS-z8-1. Other than an indication that Lyα is unusually broad, there is no evidence of a hard radiation field for COSz2; although strong He II cannot be detected due to the coincidence with a sky line, there is no evidence of C IV or N V emission. We now examine the consequences of these emission-line ratios, focusing on COSY and COSz1, using a suite of photoionization models discussed more fully in Nakajima et al. (2017). We briefly summarize the details of these simulations below.

Our photoionization models are based on *Cloudy* (version 13.03; Ferland et al. 1998, 2013) and assume constant-density gas clouds with a plane-parallel geometry. Dust physics and elemental depletion factors follow the analyses of Dopita et al. (2006) and Nagao et al. (2011). All elements except nitrogen, carbon, and oxygen, are taken to be primary nucleosynthetic products. We use the precepts given by Dopita et al. (2006) and López-Sánchez et al. (2012), respectively, to account for their

Table 4
Extracted Fluxes and Upper Limits for the Various Emission Lines with Errors Determined by Considering the Signals in Several Apertures at Similar Wavelengths (See the Text for Details)

Object	Line	$\lambda_{\text{restframe}}$ [Å]	λ_{obs} [Å]	Flux ×10^{-18} erg s^{-1} cm^{-2}	Δ_ν km s^{-1}
COSY	Lyα	1215.7	9 907.2	22.9 ± 3.0	286.6
	N V	1238.8	10 086.4	2.58 ± 0.44	17. 4
	C IV	1548.2	⋯	<2.70	
	He II	1640.0	13 360.3	1.26 ± 0.29	181.4
	C III] 1906.7 /1908.7		⋯	<0.92/<0.83	
COSz1	Lyα	1215.7	⋯	<0.96	
	N V	1238.8	⋯	<1.62	
	C IV	1548.2	⋯	<2.22	
	He II	1640.0	⋯	<2.88	
	C III] 1906.7 /1908.7		⋯/ 14 992.0	<1.18 / 1.33 ± 0.31	21. 4
COSz2	Lyα	1215.7	9502.0	9.35 ± 3.7	325.6
	N V	1238.8	⋯	<1.53	
	C IV	1548.2	⋯	<2.49	
	He II	1640.0	⋯	Sky-line	
	C III] 1906.7 /1908.7		⋯	Sky-line/<1.57	

Note. Individual detection uncertainties are 1σ and non-detection are quoted at the 3σ level. Velocity offsets are computed from the [C II] detections by ALMA (Pentericci et al. 2016; Smit et al. 2017).
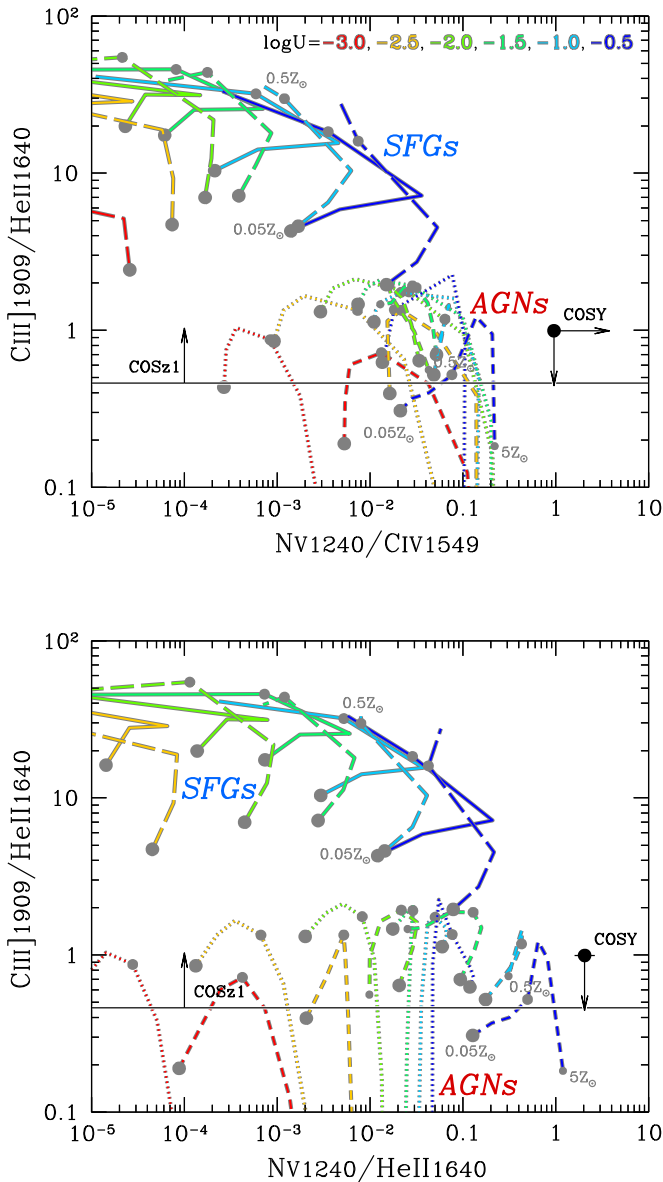
Figure 7. Line ratio diagrams from photoionization models. Metallicity ranges from $Z = 0.05$ to 1 (5) $Z_\odot$ for galaxy (AGN) models for an ionization parameter $\log(U)$ from -3.0 (red) to -0.5 (blue) as shown in the legend. Solid and long dashed lines are for single and binary stellar population models in star-forming galaxies (SFGs), respectively. Dashed and dotted curves present AGN models with power-law indices $\alpha = -1.2$ (hard) and -2.0 (soft), respectively.

secondary products. For helium, we adopt the form given by Dopita et al. (2006). The models are constructed for varying ISM properties of metallicity (Z), ionization parameter ($\log U$), and electron density.

To test the AGN hypothesis, we contrast the predictions for ionizing radiation fields from star-forming galaxies generated by stellar population synthesis codes (including both single and binary stellar evolution) and AGN with a range of power-law indices. An important caveat is that the models do not consider the effects of shocks. Although the effect of shocks on the integrated UV spectra of star-forming galaxies is expected to be modest, Jaskot & Ravindranath (2016) have shown how C III] emission can be enhanced by shocks with low velocities and

strong magnetic fields, leading to spectral signatures mimicking those of AGN.

For the radiation field from star-forming galaxies, we adopt the population synthesis code BPASS (v2; Stanway et al. 2015). We use publicly available BPASS SEDs for a Kroupa IMF under the assumption of a continuous star formation history at an age of 50 Myr. Stellar metallicities are matched to their gas-phase equivalents. Both single and binary star populations are considered.

For the AGN, we consider a narrow-line region (NLR) surrounding an AGN ionizing radiation field characterized by a power law. Our AGN models are generated by adopting an AGN continuum with the default parameters except for the power-law energy slope between the optical and X-ray bands, $\alpha_{ox} = -1.2$ and -2.0 (Zamorani et al. 1981). This parameter corresponds to the power-law index α, where $f_\nu \propto \nu^\alpha$, determined in the range of a few to a few thousand eV. The AGN models are truncated at a neutral column density of $N(HI) = 10^{21}$ cm^{-2}, in accordance with the NLR models of Kewley et al. (2013). For the AGN modes we assume dust-free gas clouds and ignore the depletion of elements onto dust grains, consistent with models that reproduce observations of high-redshift radio galaxies, type-II QSOs, and local type-II AGNs (e.g., Nagao et al. 2006).

Figure 7 compares the C III], C IV, He II, and N V line ratios for COSY and COSz1 with the full range of models for star-forming galaxies of varying metallicity Z and ionization parameter, $\log U$ and AGN models of varying power-law indices α. Since C IVλ1550.8 Å falls under a sky line, its contribution to the total C IV line flux is uncertain. However, regarding the typical ratio observed in low-z galaxies between the two components ($\sim$0.7, e.g., Berg et al. 2016; Senchyna et al. 2017), any correction to include its contribution would not change our conclusions, as the lower limit of the N V/C IV ratio would only be reduced by a factor $\sim$1.7 if the CIV1550 component, hidden by a sky line, is taken into account. In both figures, COSY is irreconcilable with a normal star-forming radiation field both on account of the low C III]/He II ratio and, especially, the strength of N V. The difficulty in explaining the line ratios in the context of star formation is also confirmed with other photoionization models such as those of Gutkin et al. (2016). Line ratios of C III]/He II $\geqslant -1$ and N V/C IV $\geqslant 1$ are only predicted for cases of high metallicity ($Z \geqslant 1 - 2Z_\odot$, Hamann & Ferland 1999), a low C/O abundance ratio (10%–20% solar) and a high ionization parameter ($\log U \simeq -1$). Such a combination is highly unlikely emphasizing the difficulty of explaining COSY with star-forming models. The prominence of N V is surprising and places it at the extreme end of the AGN predictions. Although suggestive of a high abundance, since nitrogen is a secondary element, this is not a particularly likely explanation. Conceivably, there is an additional physical mechanism involved such as the gas micro turbulence with associated dissipative heating as suggested in Kraemer et al. (2007); see also Bottorff & Ferland 2002).

For COSz1, the absence of He II and C IV provides a reasonable indication that the radiation field is consistent with a star-forming galaxy and perhaps the absence of Lyα is consistent with the source being atypical with its redder UV slope ($\beta = -1.18$) among the IRAC excess sample. Indeed, the detection of Lyα in COSz2 ($\beta = -1.72$) strengthens the

case that IRAC excess sources have unusually powerful Lyα emission.

Our spectroscopic observations of three IRAC excess $z \simeq 7$ galaxies raises several points of interest. First, it is clear how important it is to sample the full wavelength range where the key diagnostic lines occur. In the case of COSz1, Figure 7 indicates how important are constraints on other diagnostic lines in reaching any conclusion. A second aspect is the significant variation in the spectral properties of our trio of $z \simeq 7$ targets. As Table 3 reveals, all sources have similar luminosities and stellar masses yet the radiation field in COSY could not be more distinct from that in COSz1 and, probably COSz2 . Although this suggests the IRAC excess sources may not represent a uniform population, if one includes the other 3 RBS sources, the detection of Lyα in 5 out of 6 such $z > 6.8$ sources still supports the hypothesis that they lie in ionized bubbles. However, conceivably such ionized bubbles may be produced by more than one physical process as discussed by Stark et al. (2017). COSY presents a convincing case for a AGN embedded in a star-forming galaxy whereas, perhaps others in the sample may lie in an over density of sources whose collective output is the primary cause of the ionized surroundings. Further imaging of IRAC excess targets will help clarify this additional explanation.

Finally, our survey illustrates the feasibility of making further progress ahead of the launch of *JWST*. NIRSpec on *JWST* will transform studies of this kind by providing sensitive spectroscopic measures unhindered not only by the shielding effect of OH emission as in COSz2 but also the non-uniform atmospheric transmission. Such data will also, of course, finally ascertain the strength of the implied [O III] emission and, together with other rest-frame optical lines, thus provide a valuable independent constraint on the gas-phase metallicity, significantly improving the interpretation of diagrams such as Figure 7.

6. Summary

We have discussed the results from long exposure XSHOOTER spectra for three carefully selected $z \simeq 7$ targets with fairly uniform photometric properties, all characterized by a prominent flux excess in one of the IRAC bands, suggestive of intense [O III] emission. We can summarize our finding as follows.

1. Our first goal has been to determine whether the ubiquity of Lyα emission in the four RBS IRAC excess sources at $z > 7$ is a distinct property of such sources, indicating each lies in an early ionized bubble. Lyα emission is now seen in one further source and, noting the range of UV continuum slopes, we conclude the hypothesis is still supported.
2. Our second goal has been to test whether a non-thermal radiation field is responsible for the putative ionized bubbles, as suggested by the early detection of C III] and C IV in some of the RBS sources. We find a surprising diversity in the spectral characteristics of our IRAC excess sources. One (COSY) shows evidence for a hard AGN component as evidenced by broad Lyα and prominent emission lines of He II and, especially, N V. The other two are consistent with normal star-forming galaxies although uncertainties remain and COSz2 also reveals broad Lyα. This may suggest our IRAC excess

sources, which are among the most massive and luminous at these redshifts, are capable of ionizing their surroundings due to a variety of physical mechanisms, not only due to the presence of a AGN but also perhaps their location in an over density.

3. Finally, we have demonstrated the ultimate capability of ground-based spectrographs in this endeavour ahead of the launch of *JWST*. Our targets represent the brightest available in the *HST* archive, chosen carefully in a redshift range where most of the key diagnostic lines are visible. With integration times of over two nights with an efficient instrument, we have made some progress in constraining there nature of the radiation for sources well within the reionzation era.

ORCID iDs

Nicolas Laporte ◉ https://orcid.org/0000-0001-7459-6335
Kimihiko Nakajima ◉ https://orcid.org/0000-0003-2965-5070
Richard S. Ellis ◉ https://orcid.org/0000-0001-7782-7071
Adi Zitrin ◉ https://orcid.org/0000-0002-0350-4488
Ramesh Mainali ◉ https://orcid.org/0000-0003-0094-6827
G. Roberts-Borsani ◉ https://orcid.org/0000-0002-4140-1367

References

Ashby, M. L. N., Willner, S. P., Fazio, G. G., et al. 2015, ApJS, 218, 33
Berg, D. A., Skillman, E. D., Henry, R. B. C., Erb, D. K., & Carigi, L. 2016, ApJ, 827, 126
Bottorff, M., & Ferland, G. 2002, ApJ, 568, 581
Bouwens, R. J., Illingworth, G. D., Oesch, P. A., et al. 2014, ApJ, 793, 115
Castellano, M., Amorín, R., Merlin, E., et al. 2016, A&A, 590, A31

da Cunha, E., Charlot, S., & Elbaz, D. 2008, MNRAS, 388, 1595
D'Aloisio, A., Upton Sanderbeck, P. R., McQuinn, M., Trac, H., & Shapiro, P. R. 2017, MNRAS, 468, 4691
de Barros, S., Vanzella, E., Amorín, R., et al. 2016, A&A, 585, A51
Di Criscienzo, M., Merlin, E., Castellano, M., et al. 2017, A&A, 607, 30
Dopita, M. A., Fischera, J., Sutherland, R. S., et al. 2006, ApJS, 167, 177
Duncan, K., Conselice, C. J., Mortlock, A., et al. 2014, MNRAS, 444, 2960
Feltre, A., Charlot, S., & Gutkin, J. 2016, MNRAS, 456, 3354
Ferland, G. J., Korista, K. T., Verner, D. A., et al. 1998, PASP, 110, 761
Ferland, G. J., Porter, R. L., van Hoof, P. A. M., et al. 2013, RMxAA, 49, 137
Freudling, W., Romaniello, M., Bramich, D. M., et al. 2013, A&A, 559, A96
Giallongo, E., Grazian, A., Fiore, F., et al. 2015, A&A, 578, A83
Glikman, E., Djorgovski, S. G., Stern, D., et al. 2011, ApJL, 728, L26
Grogin, N. A., Kocevski, D. D., Faber, S. M., et al. 2011, ApJS, 197, 35
Gutkin, J., Charlot, S., & Bruzual, G. 2016, MNRAS, 462, 1757
Hamann, F., & Ferland, G. 1999, ARA&A, 37, 487
Japelj, J., Vanzella, E., Fontanot, F., et al. 2017, MNRAS, 468, 389
Jaskot, A. E., & Ravindranath, S. 2016, ApJ, 833, 136
Jones, T. A., Ellis, R. S., Schenker, M. A., & Stark, D. P. 2013, ApJ, 779, 52
Kawamata, R., Ishigaki, M., Shimasaku, K., Oguri, M., & Ouchi, M. 2015, ApJ, 804, 103
Kewley, L. J., Dopita, M. A., Leitherer, C., et al. 2013, ApJ, 774, 100
Koekemoer, A. M., Faber, S. M., Ferguson, H. C., et al. 2011, ApJS, 197, 36
Kraemer, S. B., Bottorff, M. C., & Crenshaw, D. M. 2007, ApJ, 668, 730
Kuraszkiewicz, J. K., & Green, P. J. 2002, ApJL, 581, L77
Laporte, N., Infante, L., Troncoso Iribarren, P., et al. 2016, ApJ, 820, 98
Leethochawalit, N., Jones, T. A., Ellis, R. S., Stark, D. P., & Zitrin, A. 2016, ApJ, 831, 152
Lehnert, M. D., van Driel, W., Le Tiran, L., Di Matteo, P., & Haywood, M. 2015, A&A, 577, A112
Leitherer, C., Schaerer, D., Goldader, J. D., et al. 1999, ApJS, 123, 3
López-Sánchez, Á R., Dopita, M. A., Kewley, L. J., et al. 2012, MNRAS, 426, 2630
Madau, P., & Haardt, F. 2015, ApJL, 813, L8
Mainali, R., Kollmeier, J. A., Stark, D. P., et al. 2017, ApJL, 836, L14
McCracken, H. J., Milvang-Jensen, B., Dunlop, J., et al. 2012, A&A, 544, A156
McLean, I. S., Steidel, C. C., Epps, H. W., et al. 2012, Proc. SPIE, 8446, 84460J

Merlin, E., Amorín, R., Castellano, M., et al. 2016, A&A, 590, A30
Mitra, S., Choudhury, T. R., & Ferrara, A. 2018, MNRAS, 473, 1416
Mostardi, R. E., Shapley, A. E., Steidel, C. C., et al. 2015, ApJ, 810, 107
Nagao, K., Okazaki, R., Nakamura, T., et al. 2011, Sci, 333, 1128
Nagao, T., Marconi, A., & Maiolino, R. 2006, A&A, 447, 157
Nakajima, K., Schaerer, D., Le Fevre, O., et al. 2017, arXiv:1709.03990
Nestor, D. B., Shapley, A. E., Kornei, K. A., Steidel, C. C., & Siana, B. 2013, ApJ, 765, 47
Oesch, P. A., Bouwens, R. J., Carollo, C. M., et al. 2010, ApJL, 709, L21
Oesch, P. A., van Dokkum, P. G., Illingworth, G. D., et al. 2015, ApJL, 804, L30
Oke, J. B., & Gunn, J. E. 1983, ApJ, 266, 713
Pentericci, L., Carniani, S., Castellano, M., et al. 2016, ApJL, 829, L11
Pentericci, L., Vanzella, E., Fontana, A., et al. 2014, ApJ, 793, 113
Planck Collaboration, Ade, P. A. R., Aghanim, N., et al. 2015, A&A, 576, A104
Reddy, N. A., Steidel, C. C., Pettini, M., Bogosavljević, M., & Shapley, A. E. 2016, ApJ, 828, 108
Roberts-Borsani, G. W., Bouwens, R. J., Oesch, P. A., et al. 2016, ApJ, 823, 143
Robertson, B. E., Ellis, R. S., Furlanetto, S. R., & Dunlop, J. S. 2015, ApJL, 802, L19
Rutkowski, M. J., Scarlata, C., Henry, A., et al. 2017, ApJL, 841, L27
Schenker, M. A., Stark, D. P., Ellis, R. S., et al. 2012, ApJ, 744, 179
Senchyna, P., Stark, D. P., Vidal-García, A., et al. 2017, MNRAS, 472, 2608
Smit, R., Bouwens, R. J., Carniani, S., et al. 2017, arXiv:1706.04614
Smit, R., Bouwens, R. J., Franx, M., et al. 2015, ApJ, 801, 122
Song, M., Finkelstein, S. L., Livermore, R. C., et al. 2016, ApJ, 826, 113
Stanway, E. R., Levan, A. J., Tanvir, N., et al. 2015, MNRAS, 446, 3911
Stark, D. P. 2016, ARA&A, 54, 761
Stark, D. P., Ellis, R. S., Charlot, S., et al. 2017, MNRAS, 464, 469
Stark, D. P., Richard, J., Siana, B., et al. 2014, MNRAS, 445, 3200
Stark, D. P., Schenker, M. A., Ellis, R., et al. 2013, ApJ, 763, 129
Torres-Peimbert, S., & Pena, M. 1984, RMxAA, 9, 107
Vanzella, E., de Barros, S., Vasei, K., et al. 2016, ApJ, 825, 41
Vasei, K., Siana, B., Shapley, A. E., et al. 2016, ApJ, 831, 38
Vernet, J., Dekker, H., D'Odorico, S., et al. 2011, A&A, 536, A105
Zamorani, G., Henry, J. P., Maccacaro, T., et al. 1981, ApJ, 245, 357
Zitrin, A., Labbé, I., Belli, S., et al. 2015, ApJL, 810, L12